Journal of Aerosol Science 118 (2018) 34–44

Contents lists available at ScienceDirect

Journal of Aerosol Science

journal homepage: www.elsevier.com/locate/jaerosci

In situ study of aggregate topology during growth of pyrolytic silica

Durgesh K. Rai[a,*], Gregory Beaucage[b,*], Karsten Vogtt[b], Jan Ilavsky[c], Hendrik K. Kammler[d]

[a] Cornell High Energy Synchrotron Source (CHESS), Cornell University, Ithaca, NY 14853, USA
[b] Materials Biomedical, Chemical, and Environmental Engineering, University of Cincinnati, Cincinnati, OH 45221, USA
[c] Advanced Photon Source, Argonne National Laboratory, Argonne, IL 60439, USA
[d] Novartis Pharma AG, Postfach, CH-4002 Basel, Switzerland

A B S T R A C T

Ramified aggregates are formed in many kinetically-limited growth processes such as in sooting flames. The structures are disordered and present a challenge to quantification. The topology of such nanomaterials is important in understanding their formation and properties. Recently, a method has been developed for the quantification of branching in aggregates using small-angle scattering. The method allows for determination of the average number of branches, branch length, short circuit path through an aggregate, aggregate total mass, aggregate polydispersity, primary particle coordination number, Sauter mean diameter, primary particle polydispersity, particle size distribution, and surface to volume ratio. In this report the new topological method is applied to in situ measurements previously published from a flame aerosol as a function of height above the burner. The topological evolution of primary and fractal structures is observed. This facilitates the understanding of growth dynamics and the structural rearrangements that occur during flame synthesis.

1. Introduction

Flame synthesis is widely used for metal-oxide nanoparticles (Pratsinis, 1998). Understanding nanoparticle growth in flames is rather difficult since such processes are highly dynamic in nature. Simulations coupled with theory and TEM analysis have been widely used. Small angle x-ray scattering (SAXS) and ultra-small angle x-ray scattering (USAXS) have been successfully employed to understand the characteristics of aggregates using scaling theories (Rai et al., 2012). In previous work we analyzed the structure of ceramic fractal aggregates grown in a flame by quantifying the mass fractal dimension, d_f, and the aggregate size using USAXS (Kammler, Beaucage, Kohls, Agashe, & Ilavsky, 2005). Since that publication a series of papers have been published elucidating the topological details of such fractal structures. This paper takes a second look at the previous measurements using the new approach which quantifies structural details of aggregates lacking long range order (Rai et al., 2012).

Mass fractal aggregates are clusters of primary particles that assemble into a structure with a mass fractal dimension, d_f, smaller than 3. For these aggregates the degree of aggregation is defined as,

$$z = k_0 \left(\frac{R_{g,f}}{d_p} \right)^{d_f} \tag{1}$$

* Corresponding authors.
E-mail addresses: dkr42@cornell.edu, raidurgesh@hotmail.com (D.K. Rai), beaucag@uc.edu, gbeaucage@gmail.com (G. Beaucage).

https://doi.org/10.1016/j.jaerosci.2018.01.006
Received 26 September 2017; Received in revised form 12 December 2017; Accepted 10 January 2018
Available online 17 January 2018
0021-8502/

where, $R_{g,f}$ is the radius of gyration of the fractal aggregate, and d_p is the Sauter mean diameter of the primary particles. k_0 is a scaling prefactor which depends on the shape of the primary particles and their connecting geometry (Heinson, Sorensen, & Chakrabarti, 2012) (Goudeli, Eggersdorfer, & Pratsinis, 2016). Many objects have similar d_f yet have dramatically different structure and formation mechanisms. For instance a crumpled sheet of paper and a randomly branched Gaussian diffusion path display a mass fractal dimension of 2.5 (Gomes, 1987). Simulations have shown that diffusion limited cluster aggregation leads to a d_f of about 1.8 (Meakin, Majid, Havlin, & Stanley, 1984; Meakin & Stanley, 1983) for clusters of large degree of aggregation, z on the order of 10,000. The mass-fractal dimension, fails to describe if the aggregate is an almost linear aggregate following a self-avoiding walk or a highly branched structure displaying local ballistic growth. For aggregates of commercial interest with z on the order of 100 significant variations in d_f are observed depending on the aggregate branch content, growth conditions, and z (Mulderig, Beaucage, Vogtt, Jiang, Jin et al., 2017). Branching controls the coordination number for the primary particles, the number of end-groups, the number of energetically-active, sharp curvature points at branches, the drag coefficient for an aggregate of a given mass, z, the tensile and shear strength of an aggregate of a given mass (Witten, Rubinstein, & Colby, 1993). For example, the drag coefficient for a graphene sheet and a Gaussian polymer chain of similar size, both of $d_f = 2$, is expected to be dramatically different due to such topological differences.

This paper reexamines previously reported in-situ USAXS studies on a premixed silica flame using a scaling model to understand branching characteristics within the fractal aggregates. Branching has been largely overlooked in the description of aggregates but it is a major distinguishing characteristic for disordered materials that can directly control engineering properties (Li et al., 2016; Raja et al., 2015). Quantification of branching reveals new details to understanding the dynamic changes during flame synthesis. This unique approach of parameterization can potentially be used to tune the manufacturing process.

2. Small angle scattering

Small angle scattering provides an azimuthally summed intensity as a function of the scattering wave vector, $q = (4\pi/\lambda)sin\theta$, where λ is the wavelength and 2θ is the scattering angle. The wave vector is reciprocal to size. Therefore, lower-q provides details of larger-sized aggregate structures while higher-q provides details of the small primary particles (Anunciado, Rai, Qian, Urban, & O'Neill, 2015; Rai et al., 2015). The two regimes may be expressed as a combination of two sets of Guinier and power laws, as shown in Fig. 1, using the Unified Fit (Beaucage, 1995, 1996, 2004; Jonah et al., 2012; Rai, 2013; Rai et al., 2012, 2016),

$$I(q) = \left\{G_f e^{-(q^2R_{g,f}^2)/3} + B_f e^{-(q^2R_{g,p}^2)/3}(q_f^*)^{-d_f}\right\} + \left\{G_p e^{-(q^2R_{g,p}^2)/3} + B_p(q_p^*)^{-4}\right\} \quad (2)$$

where, $q_i^* = q_i/\{erf\,(q_i k_{sc} R_{g,f}/\sqrt{6})\}^3$, $k_{sc} \approx 1.06$ for fractal regimes and 1 for solid particles, and erf is the error function (Beaucage, 1995). G_f and G_p are the Guinier law prefactors, B_f and B_p are the power-law prefactors and $R_{g,f}$ and $R_{g,p}$ are the radii of gyration (shown in Fig. 1), for fractal aggregates and primary particles, respectively. $-d_f$ is the slope from the power-law regime for the fractal portion of the scattering curve and is commonly known as the mass-fractal dimension which relates mass to size in real space. The Porod prefactor, B_p is obtained from Rayleigh–Gans scattering from smooth primary particles with sharp interfaces and is given by Mueller et al. (2004), Beaucage, Kammler, & Pratsinis (2004) and Rai et al. (2012),

$$B_p = 2\pi r_e^2 N(\Delta\rho)^2 S \quad (3)$$

where, r_e is the electron cross sectional radius, $\Delta\rho$ is the electron density, N is the number density of primary particles and S is the average surface area for a primary particle. The Guinier prefactor in Eq. (2) is given by Beaucage (1995, 2004), Kammler, Beaucage,

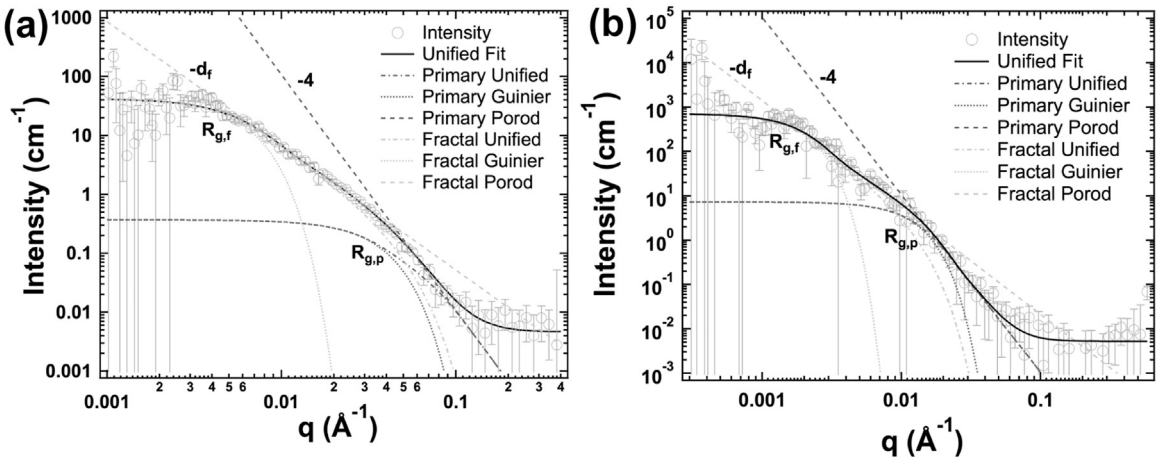

Fig. 1. In situ desmeared USAXS intensity at (a) 8 mm and (b) 100 mm HAB, in grey circles. The data was fit using Unified Fit given by Eq. (2) in solid black line. The power-law, Guinier and contribution from each level are shown in dash, dot and dash-dot respectively for the primary particle (dark grey) and fractal (light grey) regimes. The Porod-law power −4 and fractal dimension, $-d_f$, for the power laws along with respective radius of gyration from Guinier fits are indicated.

Kohls, Agashe, & Ilavsky (2005),

$$G_i = r_e^2 N(\Delta\rho)^2 V_i^2 \tag{4}$$

where, V_i is the particle or fractal aggregate occupied volume. The geometric standard deviation, σ_g, for a log-normal distribution for the spherical primary particles can be evaluated using the Guinier and Porod prefactors as, (Beaucage, Kammler, & Pratsinis, 2004)

$$\sigma_g = exp\left[\sqrt{\frac{ln\{B_p R_{g,p}^4/(1.62G_p)\}}{12}}\right] \tag{5}$$

The Porod invariant, Q, is calculated from an integral over the part of the scattering curve associated with primary particles and is given by Beaucage, Kammler and Pratsinis (2004), Beaucage, Kammler, Mueller et al. (2004), Kammler et al. (2005); Mueller et al. (2004) and Rai et al. (2012),

$$Q = \int_0^\infty q^2 I(q) dq = 2\pi^2 r_e^2 N(\Delta\rho)^2 V \tag{6}$$

The Porod invariant can be used to determine the silica volume fraction by, (Kammler et al., 2005)

$$\phi_V = \frac{Q}{2\pi^2 r_e^2 (\Delta\rho)^2} \tag{7}$$

The Porod invariant and Guinier prefactor can be used to calculate the number density of primary particles in the flame using, (Beaucage, Kammler, Mueller et al., 2004; Kammler et al., 2005; Mueller et al., 2004)

$$N = \frac{Q^2}{4\pi^4 r_e^2 (\Delta\rho)^2 G_p} \tag{8}$$

The Porod invariant and prefactor can be used to evaluate the Sauter mean diameter, d_p, of the primary particles (Beaucage, Kammler and Pratsinis, 2004; Kammler et al., 2005; Mueller et al., 2004),

$$d_p = 6\frac{Q}{\pi B_p} = 6\frac{V}{S} \tag{9}$$

The weight average number of primary particles in the aggregate, z, is obtained by Beaucage (2004), Mulderig, Beaucage, Vogtt, Jiang, and Kuppa (2017), Mulderig, Beaucage, Vogtt, Jiang, Jin et al., 2017; Rai et al., 2012),

$$z = 1 + \frac{G_f}{G_p} \tag{10}$$

3. Scaling model

The estimation of size using Guinier's law, and surface characteristics using Porod's law provides starting statistics to evaluate details of the structural topology using scaling theories. The whole aggregate composed of z primary particles with a radius of gyration of $R_{g,f}$ and a fractal dimension of d_f is deconvoluted into two conjugate sets of parameters representing the tortuosity and connectivity in the aggregate, shown in Fig. 2. The minimum path, p, is defined as an average contour path across the aggregate ignoring branches. The mass fractal dimension of the minimum path, shown in red spheres in Fig. 2, is defined as the minimum dimension, d_{min}, which can be evaluated by, (Beaucage, 2004; Rai et al., 2015)

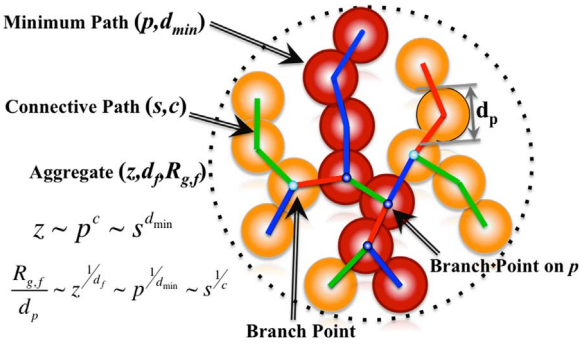

Fig. 2. Schematic representation of an aggregate structure. The aggregate contains two topologically important points, end points and branch points. Segments are portions of the structure between these topologically important points. A branch is a type of segment. The other type of segment is an inner segment between two branch points.

$$d_{min} = \frac{B_f R_{g,f}^{d_f}}{\Gamma\left(\frac{d_f}{2}\right) G_f} \tag{11}$$

where Γ is the gamma function. p and d_{min} together quantify the tortuosity of the aggregate. Larger d_{min} indicates a larger degree of convolution for the aggregate. In addition to an average minimum path, an average connectivity path can be constructed consisting of an average s primary particles represented by straight lines (in red, blue and green colors) connecting the branch points and chain end-points with a fractal dimension c that quantifies the average connectivity in an aggregate. The minimum path, p raised to the connectivity dimension, c, and the connecting path, s, raised to the tortuosity dimension, d_{min}, both represent the fractal mass or degree of aggregation, z, evaluated from Eq. (10). Therefore, we have a relation (Beaucage, 2004; Rai et al., 2012),

$$z = p^c = s^{d_{min}} \tag{12}$$

Conversely, the size of the aggregate can be obtained by reducing the respective masses by their mass dimension such that (Beaucage, 2004; Rai, 2013; Rai et al., 2012, 2015, 2016),

$$\frac{R_{g,f}}{d_p} \sim z^{\frac{1}{d_f}} \sim p^{\frac{1}{d_{min}}} \sim s^{\frac{1}{c}} \tag{13}$$

Using Eqs. (12) and (13), a connecting relationship between the two mass fractals of the conjugate sets of structures, c and d_{min}, and the mass fractal dimension of the whole aggregate, d_f, can be derived as (Beaucage, 2004),

$$d_f = c d_{min} \tag{14}$$

The branch fraction content (ϕ_{br}), which is defined as the average portion of aggregate mass which is not lying on the minimum path, shown in orange spheres in Fig. 2, is given by, (Beaucage, 2004; Rai et al., 2015; Ramachandran et al., 2012)

$$\phi_{br} = \frac{z - p}{z} = 1 - z^{\frac{1}{c}-1} \tag{15}$$

Similarly, a "meandering" fraction (ϕ_m) can also be defined that accounts for mass that is not used in direct or linear connectivity between branch- and end-points (Beaucage, 2004; Rai et al., 2015; Ramachandran et al., 2009),

$$\phi_m = \frac{z - s}{z} = 1 - z^{\frac{1}{d_{min}}-1} \tag{16}$$

The total number of branch sites in the fractal aggregate, n_{br}, shown in small spheres in Fig. 2, can be evaluated using, (Mulderig, Beaucage, Vogtt, Jiang and Kuppa, 2017; Rai et al., 2012)

$$n_{br} = \left[\frac{z^{\left\{\left(\frac{9}{4d_f} - \frac{5}{4c}\right) + \left(1 - \frac{1}{c}\right)\right\}} - 1}{2} \right] \tag{17}$$

assuming that $d_{min} = 1.8$ following diffusion limited aggregation (Meakin et al. 1984; Meakin & Stanley, 1983). Neglecting free ends (Friedlander, 2000), the average number of primary particles contacting a primary particle, which is the average coordination number, C_N, is given by Friedlander (2000); Rai et al. (2012) and Weber & Friedlander (1997),

$$C_N = 2 + \frac{n_{br}}{z} \tag{18}$$

Assuming a uniform distribution of branching points in the aggregate, the total number of branch points on the minimum path is proportional to the probability of a primary particle being a part of the minimum path and the total number of branch points, which can be evaluated as,

$$n_{br,p} = \frac{p}{z} n_{br} = n_{br} z^{-\left(1 - \frac{1}{c}\right)} \tag{19}$$

$n_{br,p}$ shown in small dark blue spheres in Fig. 2 can be used to evaluate the average branch mass or the number of particles on each branch emanating from the minimum path, $n_{br,p}$. Assuming that the branch points are trifunctional, the mass per branch, z_{br}, is given by Rai et al. (2012); Ramachandran et al. (2009),

$$z_{br} = \frac{z \phi_{br}}{n_{br,p}} \tag{20}$$

The number of inner segments, n_i, segments that connect branch points, is given by Rai et al. (2012) and Ramachandran et al. (2009),

$$n_i = n_{br} - n_{br,p} \tag{21}$$

n_i quantifies hyperbranching (branch-on-branch structure) in the aggregate. The number of segments on the minimum path, $n_{s,p}$, is numerically one more than the number of branch points on the minimum path, $n_{br,p}$, and is therefore given by Rai et al. (2012),

Table 1
Fitting and calculated scaling parameters using the Unified Fit.

Scaling parameter		*Unit*	*Scaling parameter*		*Unit*
$I(q)$	*Scattering intensity*	cm^{-1}	G_f	*Guinier's law prefactor for fractal aggregates*	cm^{-1}
q	*Scattering vector*	$Å^{-1}$	B_f	*Power-law prefactor for fractal aggregates*	$cm^{-1}\ Å^{-d_f}$
d_f	*Fractal dimesnion*	–	G_p	*Guinier's law prefactor for primary particles*	cm^{-1}
$R_{g,f}$	*Radius of gyration*	Å	B_p	*Power-law prefactor for primary particles*	$cm^{-1}\ Å^{-4}$
R_{eted}	*Aggregate end-to-end distance*	nm	z	*Number of primary particles per aggregate*	#
k_0	*Scaling prefactor*	–	z_{br}	*Number of primary particles per branch*	#
σ_g	*Geometric standard deviation*	–	z_s	*Average number of particles per segment*	#
Q	*Porod invariant*	$cm^{-1}\ Å^{-3}$	n_{br}	*Number of branch points in aggregate*	#
ϕ_V	*Silica volume fraction*	–	$n_{br,p}$	*Number of branch points on minimum path*	#
N	*Particle number density*	cm^{-3}	n_i	*Number of inner segments in aggregate*	#
d_p	*Sauter mean diameter*	nm	$n_{s,p}$	*Total number of segments on minimum path*	#
p	*Minimum path*	#	n_i	*Number of inner segments*	#
s	*Connecting path*	#	n_e	*Total number of end groups in aggregate*	#
d_{min}	*Minimum dimension*	–	$n_{s,z}$	*Total number of segments in aggregate*	#
c	*Connectivity dimension*	–	k_{min}	*Minimum shape factor*	–
ϕ_{br}	*Branch fraction*	–	k_{max}	*Maximum shape factor*	–
ϕ_m	*Meandering fraction*	–	k_{av}	*Average shape factor*	–
C_N	*Average coordination number*	#	k	*Shape factor*	–

$$n_{s,p} = n_{br,p} + 1 \tag{22}$$

The total number of end groups, n_e in analogy with the concept of free arms for polymers (Costeux, Wood-Adams, & Beigzadeh, 2002), for an average functionality of 3, is given by Rai et al. (2012),

$$n_e = n_{br} + 2 \tag{23}$$

On the other hand, the total number of segments in the aggregate, shown by sections with alternate red blue and green lines in Fig. 2, is given by,

$$n_{s,z} = 2n_{br} + 1 \tag{24}$$

which can then be used to evaluate the average number of primary particles per segment as (Rai et al., 2012),

$$z_s = \frac{z}{n_{s,z}} \tag{25}$$

Table 1 summarizes all the scaling parameters discussed in this section.

4. Shape factor

The radius of gyration for a mass-fractal aggregate, $R_{g,f}$, is related to the scaling parameters as, (Ramachandran et al., 2008)

$$R^2{}_{g,f} = \frac{k z^{2/d_f} d_p^2}{(c + 2/d_{min})(1 + c + 2/d_{min})} \tag{26},$$

where d_p is the Sauter mean diameter and k is a shape factor that depends on the asymmetry, and polydispersity of primary particles in aggregates (Goudeli et al., 2016; Heinson et al., 2012). For each aggregate, with fixed $R_{g,f}$ and d_f, a maximum and a minimum k value can be obtained by computing k for the two extreme cases, (a) a k_{min} for maximum tortuosity and minimum connectivity, $c = 1 \Rightarrow d_{min} = d_f$, and (b) a k_{max} for maximum connectivity and minimum tortuosity, $d_{min} = 1 \Rightarrow c = d_f$. Since we do not know an ad hoc value for k for fractal aggregates, a simple average/arithmetic mean of the minimum and maximum values, $k_{av} = \frac{1}{2}(k_{min} + k_{max})$, is used. k_{av} represents the effect of asymmetry in primary particles and the polydispersity of the aggregate and primary particles on the relationship between z and $R_{g,f}$ in Eq. (26) (Heinson et al., 2012).

The k (*or* k_{av}) factor from Eq. (26) may be correlated with a similar prefactor, k_0 from Eq. (1), that was proposed by Heinson et al. (2012) using,

$$k_{av} = \frac{(c + 2/d_{min})(1 + c + 2/d_{min})}{(k_0)^{2/d_f}} \Rightarrow k_0 = \left\{\frac{(c + 2/d_{min})(1 + c + 2/d_{min})}{k_{av}}\right\}^{\frac{d_f}{2}} \tag{27}$$

5. Experimental

Silica nanoparticle-producing flames were studied from saturated hexamethyldisiloxane, HMDSO, (Fluka Analytical, Sigma

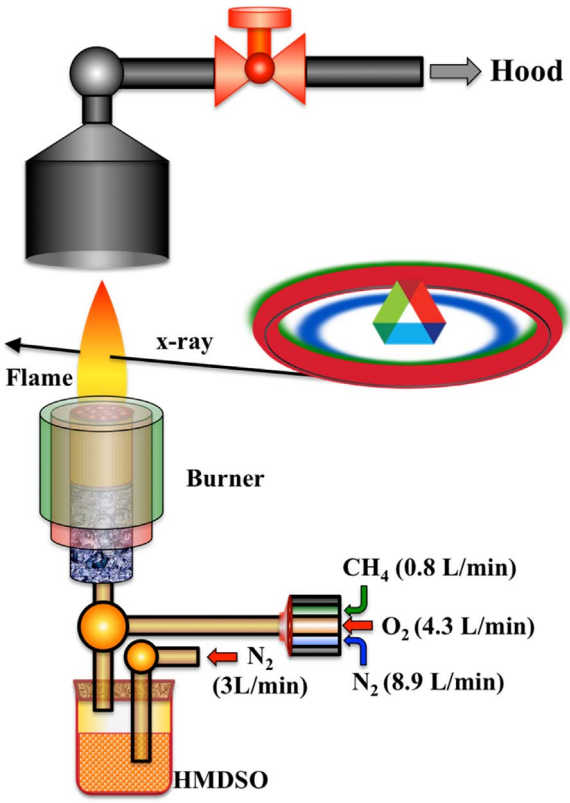

Fig. 3. Schematic representation set-up of the premixed HMDSO/methane/oxygen/nitrogen flame reactor.

Aldrich Co.) carried by nitrogen at a flow rate of 3 L/min. It was mixed with oxygen (4.3 L/min), methane (0.8 L/min) and nitrogen (8.9 L/min). A honeycomb stabilized premixed burner was used made of quartz glass with a 25 mm inner diameter as shown in Fig. 3. More details of the flame synthesis method can be found elsewhere (Beaucage, Kammler, Mueller et al., 2004; Kammler et al., 2005). The burner was fixed to a vertical/horizontal translation stage (Accudex, Aerotech Inc.) to be able to make precise axial and lateral measurements to a level of ± 0.05 mm. USAXS measurements were performed at Beamline 33ID at the Advanced Photon Source, Argonne National Laboratory. The cross-section of incident beam utilized to obtain the USAXS data was $200 \times 400\ \mu m^2$ and was oriented horizontally. The raw USAXS data was corrected for background counts, transmission and smearing (Beaucage, Kammler, Mueller et al., 2004; Kammler et al., 2005; Rai et al., 2012).

6. Results and discussion

Fig. 1 shows a typical fit to in situ data collected at 8 mm and 100 mm above the burner, from a silica premixed flame, previously published by Kammler et al. (2005). The data display two power-law decay regimes. At high-q, a Porod regime is observed that reflects the primary particle surface scattering. The associated Guinier regime labeled $R_{g,p}$ is shown at about 0.05 $Å^{-1}$. Between this high-q Guinier knee and a low-q, large size, Guinier regime, $R_{g,f}$, a power-law decay of slope ~ -2 to -2.5 is observed. This reflects branched, mass-fractal aggregates. The dashed lines in Fig. 1 reflect the components of the fit from Eq. (2).

In the premixed flame a nucleation event for silica formation occurs early in the flame. The volume fraction silica, Fig. 4(a), shows a small maximum indicating the peak in conversion from HMDSO to silica. The peak in number density of particles occurs at an earlier stage and is not discernible in this data. An observed decay in silica volume fraction, shown in Fig. 4(a), may be associated with dilution of the flame by lateral diffusion. In order to account for this dilution, the number density is reduced by the volume fraction in Fig. 4(b). This corrected number density shows a decay with HAB indicating coalescence of silica particles. This coalescence leads to a larger particle size, d_p, in Fig. 4(c), in a curve that is almost the inverse of the normalized number density curve in Fig. 4(b). Our d_p results agree reasonably well with the previously reported values (Kammler et al., 2005) but we have analyzed the whole HAB range from 8 to 100 mm instead of previously analyzed 8–40 mm. Fig. 4(b) also shows the scattering invariant (Q) as a function of HAB, which decreases before reaching a plateau above 60 mm. The Porod invariant represents the overall silica mass in the flame. The Sauter mean diameter montonically increases in Fig. 4(c). The initial growth is rapid consistent with rapid coalescence of particles early in the flame after a nucleation event. This is in contrast with Kammler et al.'s results, which seem to suggest a saturation of primary particle size above HAB of 50 mm. The early stage growth in d_p might be associated with coalescence of liquid droplets while the late stage growth in d_p might be related to clustering of solid particles by van der Waals interactions.

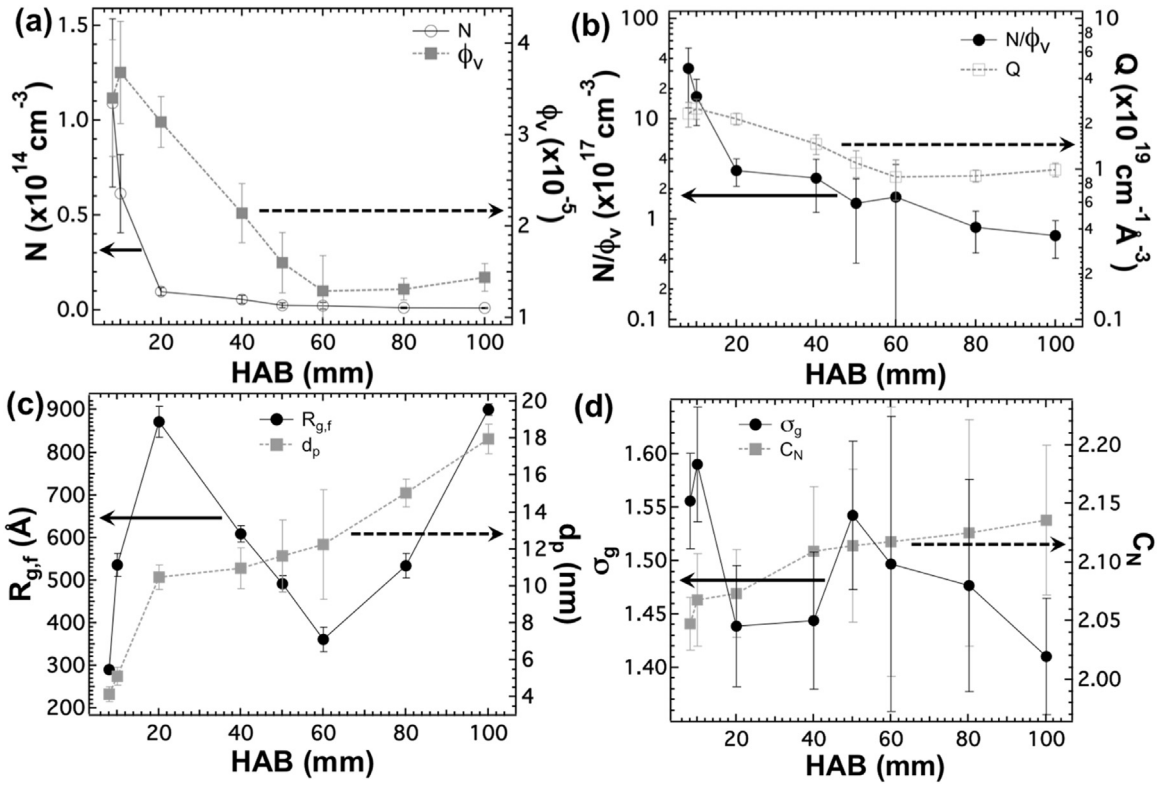

Fig. 4. (a) Primary particle number density (N) and volume fraction (ϕ_V) (b) Primary particle number density normalized by silica volume fraction (N/ϕ_V) and invariant (Q); (c) Radius of gyration, $R_{g,f}$, of aggregate and Sauter mean diameter, d_p, of primary particle; (d) Geometric standard deviation, σ_g, and average coordination number (C_N) as a function of HAB.

The geometric standard deviation of primary particles at a nucleation event is expected to be high and to drop with coalescence to a limiting values of about 1.5 for nano-scale coalescence (Friedlander, 2000), the self-preserving limit. The plot of geometric standard deviation, σ_g, for log-normal distribution for the spherical primary particles is shown in Fig. 4(d). The self-preserving limit for the nanoparticle growth is reached at ~1.44 and it increases to about ~1.60 during growth of nanoparticles (Friedlander, 2000). Fig. 4(d) shows an increase in σ_g with nucleation, followed by rapid decay with coalescence between 20 and 40 mm HAB consistent with the d_p behavior. An increase in σ_g at 50 mm HAB may be due to mixing of external streams in the flame. The results are largely consistent with the previously reported σ_g values.

After 20 mm HAB the primary particle growth slows due to the reduction in the number density of primary particles, N, lower temperature that does not favor coalescence, and sintering, and the slower diffusion rate for larger particles. While the Sauter mean diameter shows monotonic growth, the radius of gyration for the fractal structure, $R_{g,f}$, displays initial growth, followed by a decay at 20 mm HAB, and a second growth above 60 mm HAB, Fig. 4(c). The radius of gyration is calculated from the square root of the 8th to the 6th moment of the radius. These high order moments more strongly represent the larger sizes in the distribution so the curve may be misleading. The decay could be related to aggregate breakup after initial rapid growth followed by agglomeration later in the flame or it could reflect a sintering process recently shown in simulations by Eggersdorfer, Kadau, Herrmann, & Pratsinis (2012). The results for $R_{g,f}$ largely agree with those of Kammler et al. (2005). Fig. 5(a) shows fractal (d_f), connectivity (c) and minimum (d_{min}) dimensions as a function of HAB. d_f increases throughout the flame with HAB. d_f reflects the aggregate density, d_{min} the convolution of the aggregate path, and c the branch content, $d_f = cd_{min}$. An initial decrease in d_{min}, accompanied by a rapid increase in c with rapid branching at early stages of aggregate growth until HAB of 40 mm indicates a high degree of branching early in aggregate growth. After 40 mm HAB the aggregates become less branched possibly with lateral diffusion of larger aggregates of lower branch content formed in a colder part of the flame. The branching again resumes above 60 mm HAB.

Through these dimensional changes the average coordination number, C_N, in the Fig. 4(d) shows a monotonic increase indicating that branching per unit primary particle increases, Eq. (18). This can be a manifestation of changes in the average degree of aggregation during particle growth in the flame. The increase in C_N with HAB is a result of an increase in the number of branches per monomer unit or per 100 monomer units (compare Fig. 4(d) and Fig. 6(a)). d_f monotonically increases with HAB due to a complex balance between branching and convolution of the chains, as can be seen in Fig. 5(a), where $d_f = cd_{min}$. Initially, d_f increases due to increased branching parallel to c. At 40 mm HAB branching and c decrease and there is an increase in aggregate convolution and d_{min}. Finally above 60 mm HAB branching and c again increase while the aggregates become less convoluted. d_f can not be interpreted independently and must be considered with the decay in z in Fig. 5(c) and the changes in primary particle size and polydispersity in

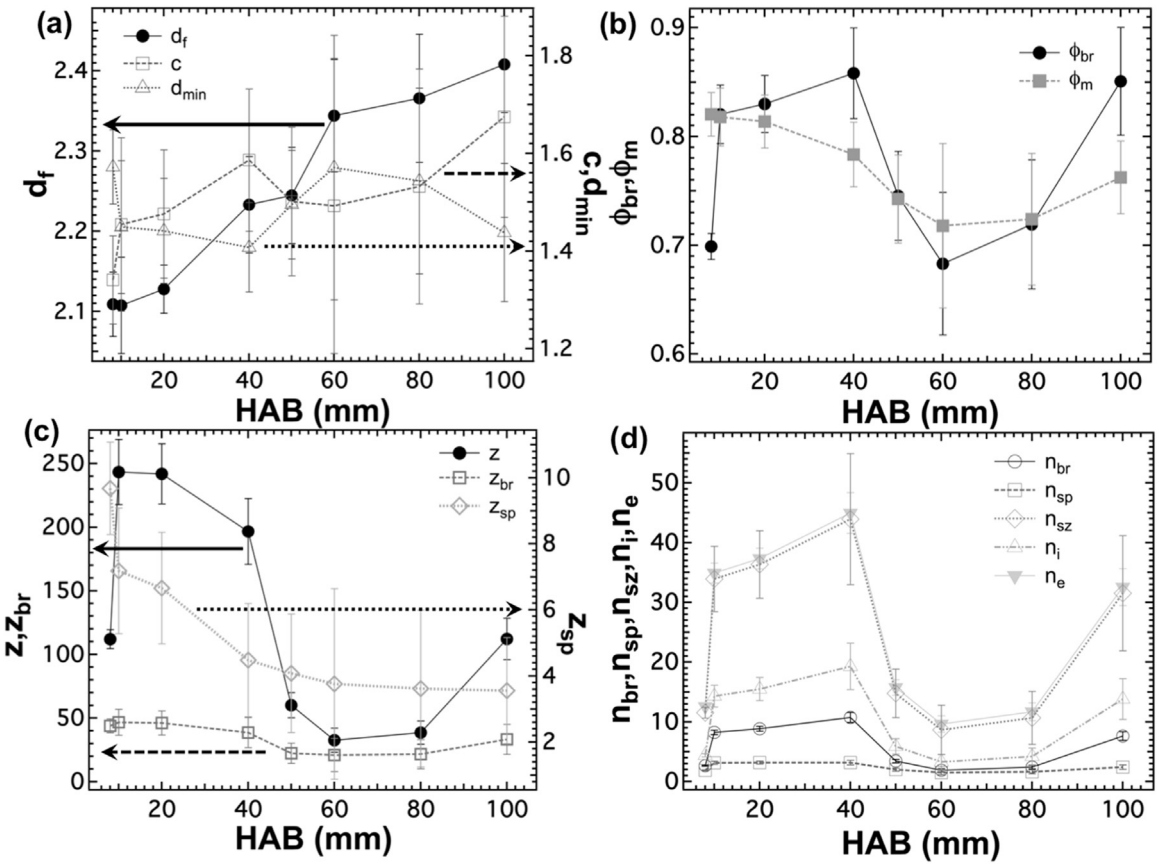

Fig. 5. *(a) Fractal (d_f), connectivity (c) and minimum dimensions of aggregate ($d_{\min}$); (b) Branch (ϕ_{br}) and meandering (ϕ_m) fractions of aggregate; (c) Weight average degree of aggregation (z), number of primary particles per branch, (z_{br}), and average number of particles per segment (z_{sp}); (d) Number of branch points in aggregate (n_{br}), number of segments in minimum path (n_{sp}), total number of segments in aggregate (n_{sz}), number of inner segments (n_i) and number of end groups per aggregate (n_e) as a function of HAB.*

Fig. 4(c) and (d).

The ratio of number density to volume fraction in Fig. 4(b) also yields the inverse of the silica volume in an average primary particle. It is expected that this will inversely follow the behavior of d_p in Fig. 4(c), which is roughly what is observed. The inverse of the ratio in Fig. 4(b) reflects a number average value while d_p is the ratio of the third to second moments. This may account for differences between the two measures.

The branch fraction (ϕ_{br}) and meandering fraction (ϕ_m) are shown as a function of HAB in Fig. 5(b). The branch fraction as well as the meandering fraction (convolution of the aggregate) decreases from 40 to 60 mm HAB, which suggest coalescence amongst the aggregates and fragmentation of the aggregates. The decrease in meandering fraction suggests that the aggregates become less convoluted until 60 mm HAB while they reduce in degree of aggregation, Fig. 5(c), z. From 40–60 mm HAB, d_p increases from 11 to about 12 nm, about a 10% increase. So some sintering occurs but not to a large extent. However, sintering is more likely in regions of high curvature such as near branch points. The number of aggregates is reflected by N/z and while N decays slowly from 40 to 60 mm HAB, z changes from 200 to about 35 in this region leading to a substantial increase in the number of aggregates probably due to fragmentation. Fragmentation might be thought to most easily occur through branch stripping since this removes an energetically unfavorable area of high negative curvature at the branch point. Also, in a shear field the removal of branches might lead to lower drag coefficient, more asymmetric aggregates. Both sintering and fragmentation might be thought to lead to a reduction in the number of branches between 40 and 60 mm HAB.

Further up stream, above 60 mm HAB, a significant increase in branching along with steady increase in convolution is observed which coincides with an increase in the aggregate dimensions and degree of aggregation, Fig. 5(c). Fig. 5(c) shows the weight average degree of aggregation (z) along with the number of primary particles per branch, (z_{br}), and the average number of particles per segment (z_{sp}) as a function of HAB. The curve for z roughly follows the curve for $R_{g,f}$. The curve for z roughly follows the curve for $R_{g,f}$. The curves support an initial increase in the degree of aggregation, which then saturates and decreases from 10 to 60 mm HAB. In comparison, the number of particles per segment monotonically decreases with HAB, z_{sp}, Fig. 5(c). The number of primaries per branch, z_{br}, varies to a relatively lesser extent with the HAB, as shown in the Fig. 5(c).

Fig. 5(d) shows the number of branch points in an aggregate (n_{br}), number of segments in a minimum path (n_{sp}), total number of segments in an aggregate (n_{sz}), the number of inner segments (n_i) and the number of end groups per aggregate (n_e) as a function of

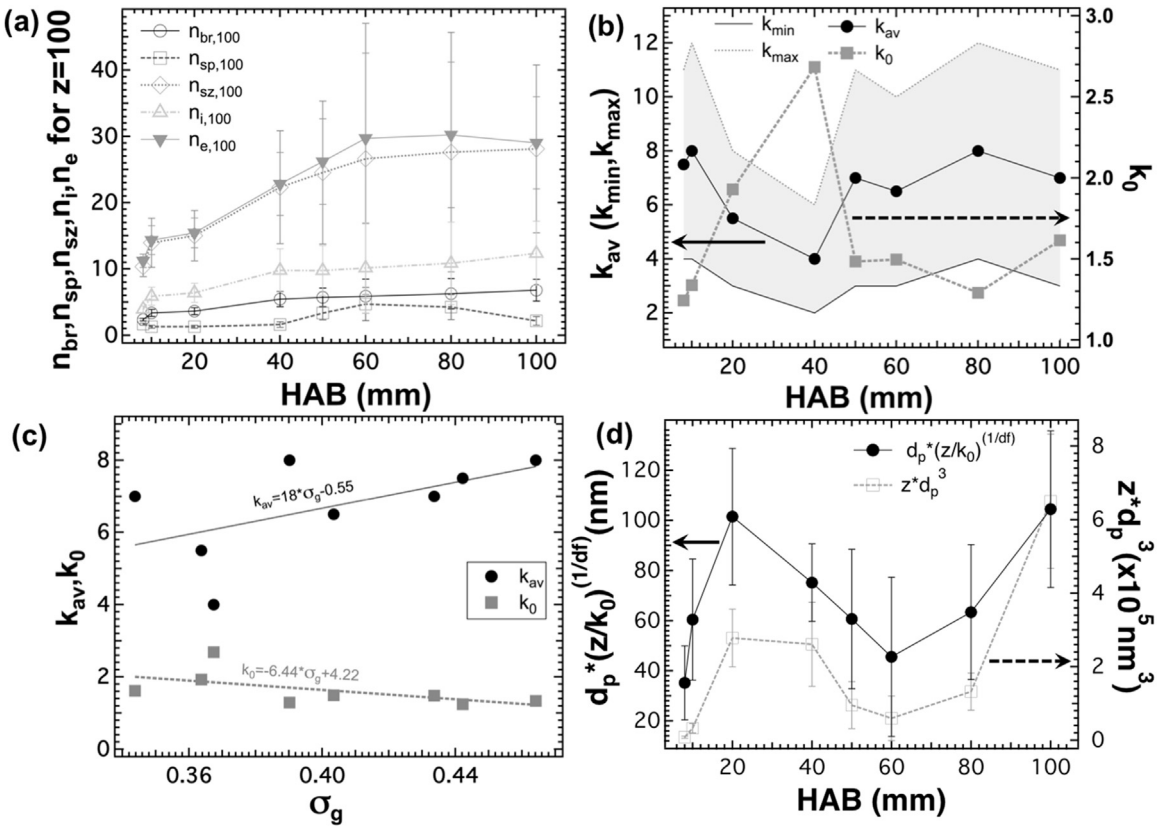

Fig. 6. (a) Normalized branching per 100 primary particles given by number of branch points in aggregate (n_{br}), number of segments in minimum path (n_{sp}), total number of segments in aggregate (n_{sz}), number of inner segments (n_i) and number of end groups per aggregate (n_e) per hundred primary particles; (b) k_{min}, $k_{\max}$ and k_{av} as a function of HAB; (c) k_{av} and k_0 as a function of σ_g. Linear fits for k_{av} and k_0 are shown in solid lines along with the fit results; (d) End-to-end distance, $R_{eted} = (z/k_0)^{1/d_f} d_p$, of aggregates on the left and degree of aggregation, multiplied by cube of Sauter mean diameter of primary particle, $zd_p{}^3$, on the right as a function of HAB.

HAB. These all essentially follow the branch fraction (ϕ_{br}) pattern. At nucleation there is a rush to branch, then the number of branches, segments and end-points remain steady before they drop after 40 mm HAB with arm breakoff and/or mixing/dilution. They all rise again high in the flame above 60 mm HAB together with a rapid growth in overall aggregate size. Nevertheless, it should be noted that the average mass of a branch, z_{br}, Fig. 5(c), always weakly decreases, which means the branches consist of a smaller number of primaries, until the end of the flame where the particles per branch slightly increases.

Another way to look at the overall architecture of aggregates is to normalize the branching numbers to a fixed number of primary particles. Fig. 6(a) shows the normalized branching per 100 primary particles given by number of branch points in aggregate (n_{br}), number of segments in minimum path (n_{sp}), total number of segments in aggregate (n_{sz}), number of inner segments (n_i) and number of end groups per aggregate (n_e) per hundred primary particles. In contrast with Fig. 5(d), the normalized number of branches, segments and end points show a steady increase throughout the growth process with increasing distance form burner, showing saturation after a HAB of 60 mm. This indicates that the structure on a primary particle basis remains similar and changes above HAB of 60 mm are largely due to changes in z.

Fig. 6(b) shows the $k_{\min}$, $k_{\max}$ and k_{av} as a function of HAB obtained from Eq. (8). As noted above, $k_{\min}$ is obtained for maximum tortuosity and minimum connectivity while $k_{\max}$ is obtained for minimum tortuosity and maximum connectivity. The k_{av} varies within ± 30% of mean. We also show the value of scattering factor, k_0, evaluated using Eq. (27) as a function of HAB. The magnitude of the k_0 parameter is largely within the range of ~1.5 except at the 40 mm HAB. This agrees rather well with the results and prediction by Heinson et al. (2012).

Fig. 6(c) shows the magnitude of k_{av} and k_0 as a function of Geometric standard deviation, σ_g. The linear fits seem to be sufficient and the trends essentially agree with the prediction from Heinson et al. (2012). So it may be inferred that the variations in the k_0 curve are similar to that of geometric standard deviation, σ_g, which would be consistent with observations reported by Goudeli et al. (2016). The shape factor for the primary particles, k_{av}, varies for aggregate materials with different asymmetry of the primary particles. A close look at Fig. 6(b) suggests that the shape of primaries changes in aspect ratio slightly, up to 30% over their growth in the flame. It is important to note that essentially any deviation from spherical geometry in primary particles would increase the surface area for the same volume, effectively decreasing d_p, which will result in a larger k_{av} factor for the same $R_{g,f}$, as long as the overall aggregate features remain the same. Therefore a change of about 30% in the shape factor due to asymmetry is possible at

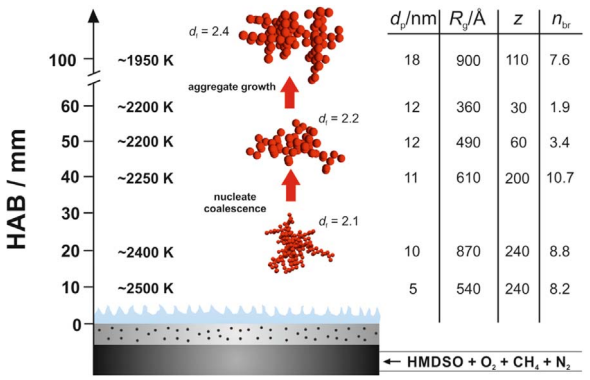

Fig. 7. Schematic diagram from topological details of growth of primary particle and fractal structures along with details of primary topological parameters with HAB. (The tabulated values are aligned with the HAB axis on the plot.).

different stages of the growth. It is also possible that the aggregate topology possibly influences the growth characteristics of the primary particles.

Fig. 6(d) shows fractal size multiplied by Sauter mean diameter, $(z/k_0)^{1/d_f} d_p$, on the left. This term reflects the aggregate end-to-end distance, R_{eted}. On the right, the degree of aggregation multiplied by the cube of the Sauter mean diameter of primary particles, zd_p^3, reflects the total mass of the aggregate, M. The end-to-end distance in Fig. 6(d), a measure of the linear size of the aggregate, and the aggregate radius of gyration, $R_{g,f}$ in Fig. 4(c) follow similar trends with rapid growth to a maximum at 20 mm HAB with initial aggregation followed by a decay to 60 mm HAB with aggregate breakup and finally a rise with aggregate-aggregate clustering above 60 mm HAB.

There are some differences between this analysis and the previous work of Kammler et al. (2005), which probably arises from the differences between the models where in branching in the aggregate is being considered in the current model while the previous approach assumed linear, unbranched chains. The current results also agree favorably with the micrographs reported by Kammler et al. (2005, Figure 3).

Fig. 7 shows a schematic of major events during the aggregate growth process. It represents topological details of the growth of primary particle and fractal structures along with details of primary topological parameters as a function of HAB. It can be useful to divide the whole aggregate growth process into different subsets based on HABs to simplify an understanding of the details of the growth process. The first stage involves the initial nucleation and rapid growth in number of primaries, degree of aggregation, silica mass density until about 8 mm HAB. Thereafter, above 8–20 mm HAB, the primaries coalesce, aggregates grow in size and degree of aggregation. The branching of the aggregates increase within this range of HAB. Thereafter, coalescence of primaries stops at 20 mm HAB since the number density normalized by silica volume fraction (N/ϕ_V) becomes constant above that point. In fact the N/ϕ_V plot in Fig. 4(d) shows that there is no influx of other streams since it is constant above 20 mm HAB. From 20–40 mm HAB, the aggregates branch while their mass (za_p^3) remains constant. The aggregate end-to-end distance, $(z/k_0)^{1/d_f} d_p$ as well as the $R_{g,f}$ decreases. From 40–60 mm HAB, the overall size as well as the mass of the aggregates drops while the branching decreases, which may be an indication that the arms may be being detached from the aggregates due to shear flow and collision. Finally from 60 to 100 mm HAB, the aggregates as well as branches grow again while the normalized number density, N/ϕ_V, keeps decreasing. This could possibly indicate agglomeration of aggregates high in the flame.

In addition, there are some universal trends that occur in the flame. For example, the mass of the branches decreases with increasing HAB. This means that branches that are created at higher HABs are comprised of comparatively fewer primary particles, until the end of the flame where larger branches grow. The change in the geometric standard deviation, σ_g, supports the proposed mechanism of aggregate growth. Many of these features are consistent with simulations of aggregate growth by Eggersdorfer et al. (2012) and Eggersdorfer & Pratsinis (2013) where the sintering process leads to a decrease in branching.

7. Conclusions

Insight into the stages of growth of ramified aggregates was presented using in-situ SAXS studies on flame synthesized silica aggregates as a function of height above burner. USAXS analysis using the Unified Fit revealed intrinsic details where the growth process could be obtained by evaluating the minimum paths, branch fractions, average number of branches, branch length, aggregate total mass, primary particle coordination number, Sauter mean diameter and primary particle polydispersity. It is possible to summarize the growth process in three steps where the initial nucleation rapid growth is followed by coalescence as the flame cools down. Thereafter at higher HABs, agglomeration of aggregates takes place resulting in larger aggregates.

Acknowledgement

This research used resources of the Advanced Photon Source, a U.S. Department of Energy (DOE) Office of Science User Facility operated for the DOE Office of Science by Argonne National Laboratory under Contract no. DE-AC02-06CH11357. G.B. and D.K.R.

were supported by the NanoPower Africa Project funded by United States Agency for International Development (USAID) through the Higher Education for Development (HED) office, USAID/South Africa Associate Award Cooperative Agreement #AEG-A-00-05-00007-00 Associate Cooperative Agreement #674-A-00-11-00018-00. This paper is made possible by the generous support of the American people through the USAID and the HED office. The contents are the responsibility of the authors and do not necessarily reflect the views of HED, USAID or the United States Government. DKR is also supported by Cornell High Energy Synchrotron Source (CHESS), which is supported by the National Science Foundation and the National Institutes of Health/National Institute of General Medical Sciences under NSF award DMR-0936384 and the Macromolecular Diffraction at CHESS (MacCHESS) facility, which is supported by award GM-103485 from the National Institutes of Health, through its National Institute of General Medical Sciences. GB was supported by the National Science Foundation through grant CMMI-1635865.

References

Anunciado, D., Rai, D. K., Qian, S., Urban, V., & O'Neill, H. (2015). Small-angle neutron scattering reveals the assembly of alpha-synuclein in lipid membranes. *Biochimica Et Biophysica Acta-Proteins and Proteomics, 1854*(12), 1881–1889. http://dx.doi.org/10.1016/j.bbapap.2015.08.009.

Beaucage, G. (1995). Approximations leading to a unified exponential power-law approach to small-angle scattering. *Journal of Applied Crystallography, 28*, 717–728.

Beaucage, G. (1996). Small-angle scattering from polymeric mass fractals of arbitrary mass-fractal dimension. *Journal of Applied Crystallography, 29*, 134–146.

Beaucage, G. (2004). Determination of branch fraction and minimum dimension of mass-fractal aggregates. *Physical Review E, 70*(3), 031401 (doi: 03140110.1103/PhysRevE.70.031401).

Beaucage, G., Kammler, H. K., Mueller, R., Strobel, R., Agashe, N., Pratsinis, S. E., & Narayanan, T. (2004). Probing the dynamics of nanoparticle growth in a flame using synchrotron radiation. *Nature Materials, 3*(6), 370–374. http://dx.doi.org/10.1038/nmat1135.

Beaucage, G., Kammler, H. K., & Pratsinis, S. E. (2004). Particle size distributions from small-angle scattering using global scattering functions. *Journal of Applied Crystallography, 37*, 523–535. http://dx.doi.org/10.1107/s0021889804008969.

Costeux, S., Wood-Adams, P., & Beigzadeh, D. (2002). Molecular structure of metallocene-catalyzed polyethylene: Rheologically relevant representation of branching architecture in single catalyst and blended systems. [Article]. *Macromolecules, 35*(7), 2514–2528. http://dx.doi.org/10.1021/ma011432c.

Eggersdorfer, M. L., Kadau, D., Herrmann, H. J., & Pratsinis, S. E. (2012). Aggregate morphology evolution by sintering: Number & diameter of primary particles. *Journal of Aerosol Science, 46*, 7–19. http://dx.doi.org/10.1016/j.jaerosci.2011.11.005.

Eggersdorfer, M. L., & Pratsinis, S. E. (2013). Restructuring of aggregates and their primary particle size distribution during sintering. *AIChE Journal, 59*(4), 1118–1126. http://dx.doi.org/10.1002/aic.14043.

Friedlander, S. K. (2000). *Smoke, dust, and haze: Fundamentals of aerosol dynamics* (2nd ed.). USA: Oxford University Press.

Gomes, M. A. F. (1987). Fractal geometry in crumpled paper balls. *American Journal of Physics, 55*(7), 649–650. http://dx.doi.org/10.1119/1.15094.

Goudeli, E., Eggersdorfer, M. L., & Pratsinis, S. E. (2016). Coagulation of agglomerates consisting of polydisperse primary particles. *Langmuir, 32*(36), 9276–9285. http://dx.doi.org/10.1021/acs.langmuir.6b02455.

Heinson, W. R., Sorensen, C. M., & Chakrabarti, A. (2012). A three parameter description of the structure of diffusion limited cluster fractal aggregates. *Journal of Colloid and Interface Science, 375*(*1*), 65–69. http://dx.doi.org/10.1016/j.jcis.2012.01.062.

Jonah, E. O., Britton, D. T., Beaucage, P., Rai, D. K., Beaucage, G., Magunje, B., ... Härting, M. (2012). Topological investigation of electronic silicon nanoparticulate aggregates using ultra-small-angle X-ray scattering. *Journal of Nanoparticle Research, 14*(*11*), 1–10. http://dx.doi.org/10.1007/s11051-012-1249-y.

Kammler, H. K., Beaucage, G., Kohls, D. J., Agashe, N., & Ilavsky, J. (2005). Monitoring simultaneously the growth of nanoparticles and aggregates by in situ ultra-small-angle x-ray scattering. *Journal of Applied Physics, 97*(*5*), 11 (doi: 05430910.1063/1.1855391).

Li, C. C., Yang, W., Zhou, W. Q., Zhang, M. M., Xue, R. Y., Li, M. Y., & Cheng, Z. Q. (2016). Branching effect for aggregation-induced emission in fluorophores containing imine and triphenylamine structures. *New Journal of Chemistry, 40*(10), 8837–8845. http://dx.doi.org/10.1039/c6nj01558a.

Meakin, P., Majid, I., Havlin, S., & Stanley, H. E. (1984). Topological properties of diffusion limited aggregation and cluster–cluster aggregation. *Journal of Physics a-Mathematical and General, 17*(18), L975–L981.

Meakin, P., & Stanley, H. E. (1983). Spectral dimension for the diffusion-limited aggregation model of colloid growth. *Physical Review Letters, 51*(16), 1457–1460.

Mueller, R., Kammler, H. K., Pratsinis, S. E., Vital, A., Beaucage, G., & Burtscher, P. (2004). Non-agglomerated dry silica nanoparticles. *Powder Technology, 140*(1–2), 40–48. http://dx.doi.org/10.1016/j.powtec.2004.01.004/.

Mulderig, A., Beaucage, G., Vogtt, K., Jiang, H., Jin, Y., Clapp, L., & Henderson, D. C. (2017). Structural emergence in particle dispersions. *Langmuir*. http://dx.doi.org/10.1021/acs.langmuir.7b03033.

Mulderig, A., Beaucage, G., Vogtt, K., Jiang, H., & Kuppa, V. (2017). Quantification of branching in fumed silica. *Journal of Aerosol Science, 109*, 28–37. http://dx.doi.org/10.1016/j.jaerosci.2017.04.001.

Pratsinis, S. E. (1998). Flame aerosol synthesis of ceramic powders. *Progress in Energy and Combustion Science, 24*(3), 197–219. http://dx.doi.org/10.1016/s0360-1285(97)00028-2.

Rai, D. K. (2013). *Quantification of fractal systems using small angle scattering (PhD Doctoral dissertation)*. University of Cincinnati〈http://rave.ohiolink.edu/etdc/view?acc_num=ucin1377870724〉.

Rai, D. K., Beaucage, G., Jonah, E. O., Britton, D. T., Sukumaran, S., Chopra, S., ... Harting, M. (2012). Quantitative investigations of aggregate systems. *The Journal of Chemical Physics, 137*(*4*), 044311–044316.

Rai, D. K., Beaucage, G., Ratkanthwar, K., Beaucage, P., Ramachandran, R., & Hadjichristidis, N. (2015). Determination of the interaction parameter and topological scaling features of symmetric star polymers in dilute solution. *Physical Review E, 92*(1), 012602.

Rai, D. K., Beaucage, G., Ratkanthwar, K., Beaucage, P., Ramachandran, R., & Hadjichristidis, N. (2016). Quantification of interaction and topological parameters of polyisoprene star polymers under good solvent conditions. *Physical Review E, 93*(5), 052501.

Raja, S. N., Olson, A. C. K., Limaye, A., Thorkelsson, K., Luong, A., Lin, L., ... Alivisatos, A. P. (2015). Influence of three-dimensional nanoparticle branching on the Young's modulus of nanocomposites: Effect of interface orientation. *Proceedings of the National Academy of Sciences, 112*(21), 6533–6538. http://dx.doi.org/10.1073/pnas.1421644112.

Ramachandran, R., Beaucage, G., Kulkarni, A. S., McFaddin, D., Merrick-Mack, J., & Galiatsatos, V. (2008). Persistence length of short-chain branched polyethylene. *Macromolecules, 41*(24), 9802–9806. http://dx.doi.org/10.1021/ma801775n.

Ramachandran, R., Beaucage, G., Kulkarni, A. S., McFaddin, D., Merrick-Mack, J., & Galiatsatos, V. (2009). Branch content of metallocene polyethylene. *Macromolecules, 42*(13), 4746–4750. http://dx.doi.org/10.1021/ma900199t.

Ramachandran, R., Beaucage, G., Rai, D. K., Lohse, D. J., Sun, T., Tsou, A. H., & Hadjichristidis, N. (2012). Quantification of branching in model three-arm star polyethylene. *Macromolecules, 45*(2), 1056–1061. http://dx.doi.org/10.1021/ma2021002.

Weber, A. P., & Friedlander, S. K. (1997). Relation between coordination number and fractal dimension of aerosol agglomerates. *Journal of Aerosol Science, 28*(SUPPL. 1), S765–S766.

Witten, T. A., Rubinstein, M., & Colby, R. H. (1993). Reinforcement of rubber by fractal aggregates. *Journal de Physique, 3*(3), 367–383.